ACSNANO
Cite This: ACS Nano 2019, 13, 3196−3205
www.acsnano.org

MoS_2-Based Optoelectronic Gas Sensor with Sub-parts-per-billion Limit of NO_2 Gas Detection

Tung Pham,[†,∥] Guanghui Li,[†,§,∥] Elena Bekyarova,[†,‡,§] Mikhail E. Itkis,*[,†,‡,§] and Ashok Mulchandani*[,†,⊥]

[†]Department of Chemical and Environmental Engineering, [‡]Department of Chemistry, [⊥]Materials Science and Engineering Program, and [§]Center for Nanoscale Science and Engineering, University of California, Riverside, California 92521, United States

Supporting Information

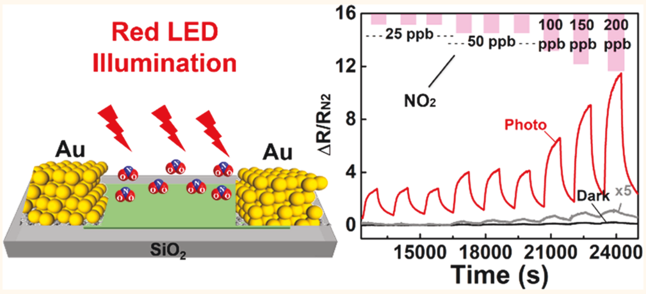

ABSTRACT: **Red light illumination with photon energy matching the direct band gap of chemical vapor deposition grown single-layer MoS_2 with Au metal electrodes was used to induce a photocurrent which was employed instead of dark current for NO_2 gas sensing. The resulting Au/MoS_2/Au optoelectronic gas sensor showed a significant enhancement of the device sensitivity S toward ppb level of NO_2 gas exposure reaching S = 4.9%/ppb (4900%/ppm), where S is a slope of dependence of relative change of the sensor resistance on NO_2 concentration. Further optimization of the MoS_2-based optoelectronic gas sensor by using graphene (Gr) with a work function lower than that of Au for the electrical contacts to the MoS_2 channel allowed an increase of photocurrent. The limit of detection of NO_2 gas at the level of 0.1 ppb was obtained for the MoS_2 channel with graphene electrodes coated by Au. This value was calculated using experimentally obtained sensitivity and noise values and exceeds the U.S. Environment Protection Agency requirement for NO_2 gas detection at ppb level.**

KEYWORDS: *2D material, transition metal dichalcogenides, MoS_2, graphene, optoelectronic, photogating, gas sensor*

Following the discovery of graphene,[1] other two-dimensional (2D) materials such as transition metal dichalcogenides (TMDs) have attracted significant attention because of the unique electronic properties originated from their low-dimensional electronic structure.[2−6] In contrast to graphene, TMDs possess finite band gap in the range from 0.2 to 3 eV, depending on specific type of material and number of layers and became a valuable alternative to the conventional or narrow band semiconductors in a variety of electronic and optoelectronic applications.[2−7] MoS_2 is one of the most prominent materials from the TMD family possessing a direct band gap of 1.8 eV as a single layer[8,9] and showing promising performance in field-effect transistors (FETs), p−n junctions and heterojunctions, photovoltaic cells, and photodetectors.[10−15]

Because of their high surface to volume ratio, electronic transport in atomically thin TMD channels is extremely sensitive to the surrounding atmosphere, thus allowing their exploration in chemical and biological molecule sensing applications.[16−22] TMDs are now considered as promising alternatives to the conventional metal oxide sensing materials,[23−26] which typically require elevated temperature operations causing excessive energy consumption, reliability issues, and safety concerns. Chemiresistors based on single- and multilayer MoS_2, either mechanically exfoliated or chemical vapor deposition (CVD)-grown, have been explored for sensing of such hazardous analytes as NO, NH_3, volatile organic compounds (VOCs), and nerve agents at ppm level.[16−22] Nitrogen dioxide (NO_2) is one of the most dangerous pollutants produced mainly as a byproduct of combustion reaction in transportation and industrial processes.[27] It is reported that exposure to as small concentration as 3 ppm can lead to eye and lung irritation, lower resistance to respiratory infection, and possible fatality.[23] In addition, NO_2 can react with other chemicals in ambient atmosphere to form acid rain and ozone, which are the major harmful components to most ecosystems. Due to such negative impacts to both environment and human life, the United States Environmental Protection Agency (U.S. EPA) has regulated limit of exposure to NO_2 at 53 ppb,[28] thus leading to urgent need to develop a highly sensitive and real-time operating NO_2 gas sensors performing reliably at ppb level.

Received: November 18, 2018
Accepted: February 20, 2019
Published: February 20, 2019

DOI: 10.1021/acsnano.8b08778
ACS Nano 2019, 13, 3196−3205

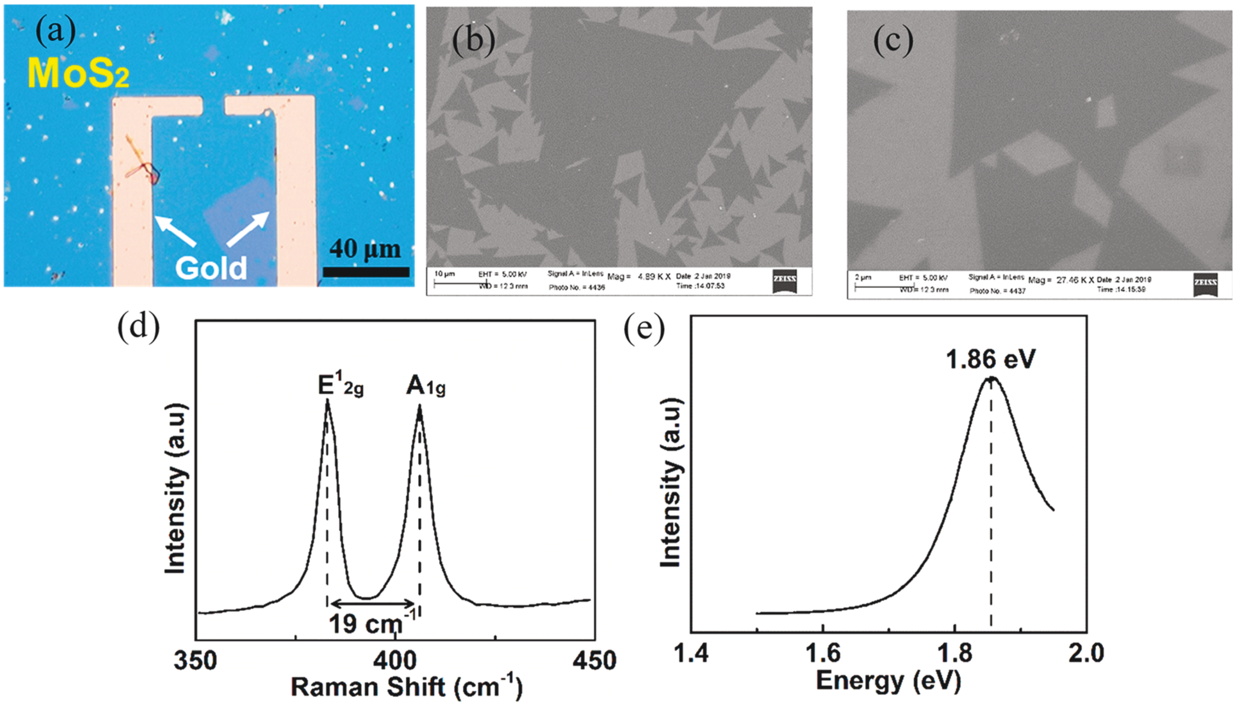

Figure 1. (a) Optical image of MoS_2 device with Au electrodes. (b,c) SEM images of MoS_2 layer at different magnifications with MoS_2 corresponding to lighter areas (scale bars 10 and 2 μm, respectively). (d) Raman and (e) photoluminescence spectra of MoS_2 layer.

In recent years, a number of studies demonstrated efficient MoS_2-based NO_2 sensor performances at ppm level.[20,21,29] Moreover, it has been reported recently that a CVD-grown MoS_2 FET-based gas sensor is capable for NO_2 detection at sub-ppm (200 ppb) level.[20] However, these sensors had a slow response and poor recovery at room temperature. Later reports show improved recovery by utilization of elevated temperatures ranging from 100 to 150 °C due to accelerated desorption of the gas molecules.[30,31] As an alternative strategy, UV light irradiation of the MoS_2 channel was employed to improve sensitivity and recovery rate of the response to NO_2 exposure at ppm level[29] following the strategy developed earlier for metal-oxide-based sensors.[32,33] In that report,[29] UV light is used as a tool to release oxygen ions from the MoS_2 surface, thus facilitating the interaction of NO_2 molecules with conducting electrons in the MoS_2 channel and yielding faster removal rate of NO_2 molecules after the exposure.

The MoS_2 sensing channel can be prepared in different morphologies such as mechanically exfoliated single- or multilayered,[16,18] MoS_2 nanowire networks[34] or horizontally and vertically aligned MoS_2 layers.[35,36] Each of those morphologies provides significant input in the development of MoS_2-based sensing technology. CVD-grown single-layer MoS_2 is an ultimate 2D material with highest possible surface to volume ratio and is more suited for semiconducting processing platforms. However, due to several factors such as large band gap of MoS_2, grain boundaries of MoS_2 triangular crystals forming its single-layer structure, and contribution of Schottky barriers at metal–MoS_2 contact interfaces, the typical sensor resistance can reach extremely high values of 10 GΩ to 1 TΩ. This complicates the sensor's electrical integration with readout circuit and increases electrical noise, thus degrading the sensor performance in terms of limit of detection of gaseous analytes.

Here, we utilize light-emitting diode (LED) illumination with photon energy matching the band gap of single-layer MoS_2 in order to decrease the MoS_2 channel resistance by 3 orders of magnitude by inducing a photocurrent and employing the generated photocurrent instead of dark current for NO_2 gas sensing. As a result, an efficient response to sub-ppm level of NO_2 concentrations (25–200 ppb) exposure was demonstrated with a sensitivity of 4.9%/ppb (4900%/ppm). Further optimization of the MoS_2-based optoelectronic gas sensor by using graphene (Gr) with a work function lower than that of Au for the electrical contacts to the MoS_2 channel allowed an increase of photocurrent and improving signal to noise ratio of the gas detection. Calculations of the optimized chemi-photoresistor limit of detection (LOD) following IUPAC procedure,[37] provided an evaluation of LOD for NO_2 detection at the level of ~0.1 ppb, which by far exceeds the U.S. EPA requirement of NO_2 detection at ppb level.

RESULTS AND DISCUSSION

Figure 1a presents an optical image of the MoS_2 optoelectronic gas sensor with two patterned Au electrodes with 10 μm by 10 μm gap. Figure 1b,c shows scanning electron microscopy (SEM) imaging of a MoS_2 layer forming the device channel with typical morphology of one atomic layer network of merging triangular MoS_2 crystals. Detailed information on MoS_2 layer growth and the device preparation is presented in the Experimental Section. Raman spectrum of MoS_2 (Figure 1d) shows E^1_{2g} peak at 386 cm^{-1} and A_{1g} peak at 405 cm^{-1} in a ratio of $E^1_{2g}/A_{1g} \approx 1$, indicating a basal plane exposed morphology.[34,35] Those peaks are separated by 19 cm^{-1}, in agreement with the expected value for a single-layer MoS_2.[8,9] The presence of strong photoluminescence peak at 1.86 eV photon energy (Figure 1e) confirms that the device channel is predominantly single-layer MoS_2.[8]

DOI: 10.1021/acsnano.8b08778
ACS Nano 2019, 13, 3196–3205

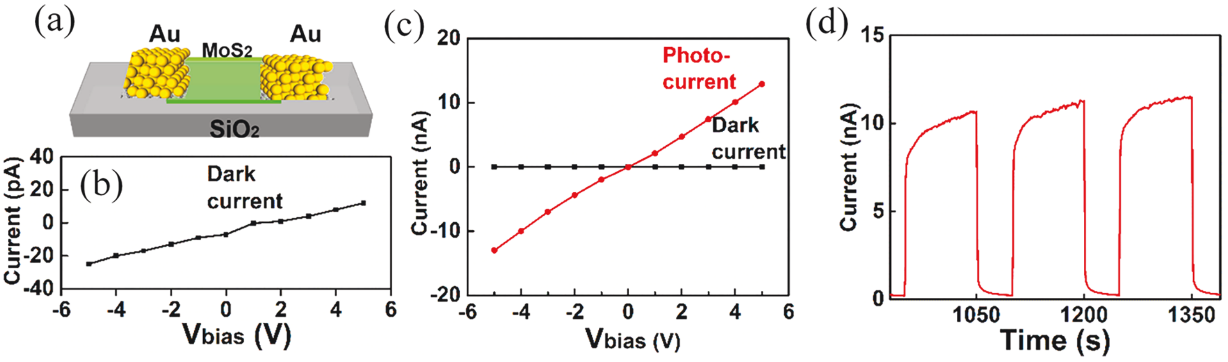

Figure 2. (a) Schematic of MoS_2 channel with Au electrodes; $I-V$ dependence of the Au−MoS_2−Au device (b) in the dark and (c) under red LED illumination with incident power of 60.9 nW; (d) photocurrent pulses as a response to "on" and "off" switching of red LED irradiation.

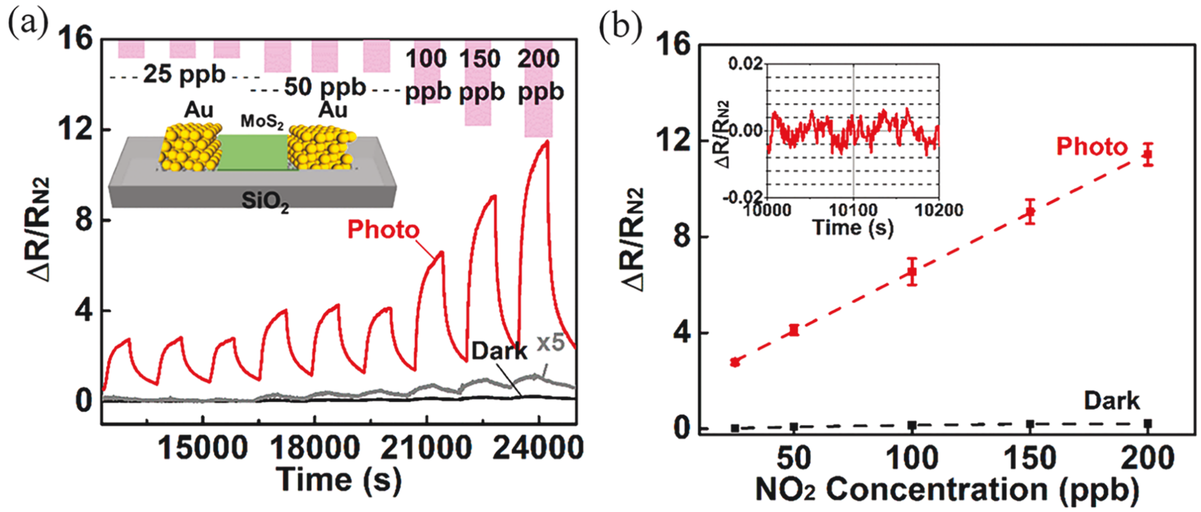

Figure 3. (a) Effect of NO_2 gas exposure at concentrations from 25 to 200 ppb on normalized resistance of the Au−MoS_2−Au device in the dark (black line; gray line shows 5-fold magnified data) and under red LED illumination (red curve). (b) Dependence of the normalized amplitude of resistance change $\Delta R/R_{N2}$ on the concentration of NO_2 gas. Inset shows a temporal trace of experimentally recorded noise of $\Delta R/R_{N2}$ under LED illumination. All data were collected under DC bias of 5 V.

Figure 2a shows a schematic of the MoS_2 channel with Cr/Au electrodes denoted in this paper as the Au−MoS_2−Au device. The $I-V$ curve in the dark (Figure 2b) shows very low current in the picoamperes range corresponding to the very high device resistance of ∼200 GΩ. Such high device resistance is due to the presence of two Schottky diode type Au/MoS_2 junctions connected in series in opposite directions, so the current through the channel is always limited by the Schottky diode which is biased in reverse. In most of our measurements, the bias across the device is limited to 5 V, whereas at higher voltages, the devices show nonlinearity associated with reverse breakdown typical for Schottky diodes (Figure S1). Under illumination of a red LED with an incident power of 60.9 nW (light intensity of 60.9 mW/cm^2), the channel current increased by ∼500 times, exceeding 10 nA at 5 V channel bias (Figure 2c).

The temporal evolution of the photocurrent when LED irradiation was switched "on" and "off" is presented in Figure 2d. It shows a relatively fast rise of the photocurrent to ∼80% level in less than 1 s when LED irradiation was switched "on" followed by a slow increase continuing for hundreds of seconds. A similar shape was observed in the photocurrent decay when LED was turned "off" with an initial fast decay to below 10% level in less than 1 s followed by a slow decay.

We next investigated the ability of the above device as a gas sensor for NO_2. Figure 3a compares typical responses of single-layer MoS_2-based gas sensors with Cr/Au electrodes (from here on referred to as Au−MoS_2−Au) to NO_2 gas exposure in the dark and under red LED illumination with incident power of 60.9 nW (light intensity of 60.9 mW/cm^2). The sensor response is represented in terms of normalized change of resistance, $\Delta R/R_{N2}$, where R_{N2} is the resistance of the device established under N_2 flow before NO_2 exposure in the dark or under illumination and ΔR is a resistance change caused upon NO_2 exposure. For raw resistance data, please see Figures S2 and S3 in the Supporting Information. It is worth noting that the sensor exhibited similar sensitivity to NO_2 even when air was used as the carrier/dilution gas instead of nitrogen (data not shown).

Noticeably, the response to NO_2 exposure under illumination is enhanced dramatically even when the dark current data are magnified by a factor of 5. Figure 3b presents the amplitude of relative response $\Delta R/R_{N2}$ in the dark and under illumination as a function of NO_2 concentration C (ppb) with a slope of such dependence defining the device sensitivity $S = \Delta R/R_{N2}(\%)/C(\text{ppb})$. Under red LED illumination, the NO_2 sensitivity of S = 4.9%/ppb (4900%/ppm) was observed, which is ∼50-fold higher than the best values of 0.1%/ppb

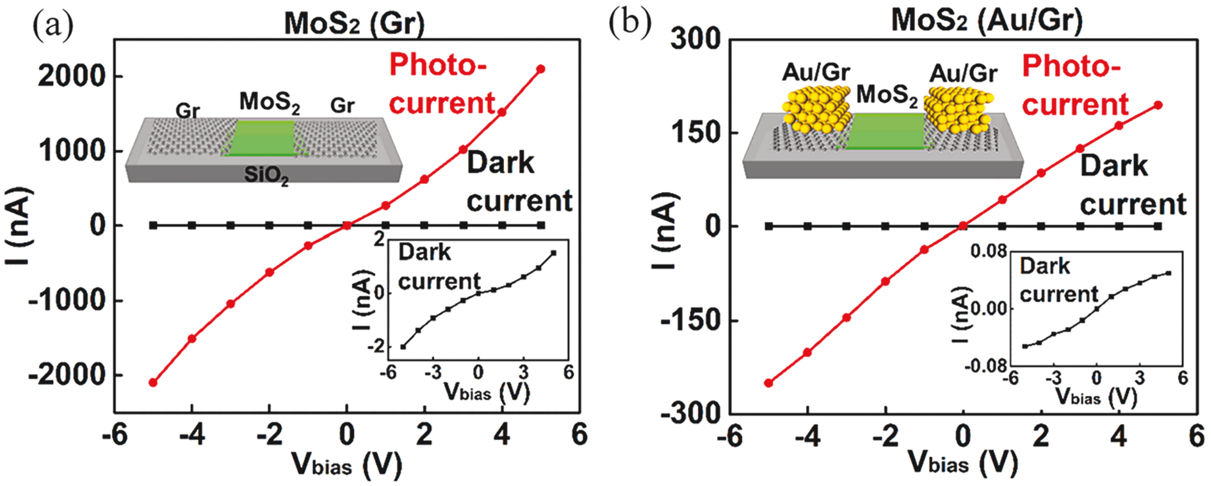

Figure 4. *I*−*V* curves under red LED illumination (red line) and in the dark (black line) of (a) Gr−MoS_2−Gr and (b) Au/Gr−MoS_2−Gr/Au devices. Insets show corresponding schematics of the devices and expanded *I*−*V* curves in the dark.

obtained in the dark. Some of the tested Au−MoS_2−Au sensors did not show any response in the dark to sub-ppm concentrations of NO_2, whereas the sensitivity under red LED light illumination was consistently high. It should be noted that the sensitivity is usually normalized to the concentration expressed in ppm units; however, in our work, we report sensitivity in %/ppb units due to the strong response of our sensor to ppb level concentration of NO_2.

Another important figure of merit of the chemical sensor is the LOD of the particular analyte which, following IUPAC procedure, is typically defined as a concentration of the analyte which causes a response 3 times higher than the noise level of the device (*i.e.*, in the absence of the analyte).[37,38] From the noise data presented in Figure 3b (inset) for the illuminated sensor, root-mean-square value of $\Delta R/R_{N2}$ noise of ∼0.32% is obtained, giving a calculated LOD of $3 \times 0.32/4.9 \approx 0.2$ ppb. For comparison, the noise level for the sensor in the dark is ∼0.6% with much lower sensitivity of 0.1%/ppb, resulting in a detection limit of $3 \times 0.6/0.1 \approx 18$ ppb, in agreement with the visual observation of data presented in Figure 3. Thus, band gap matching illumination of the MoS_2 sensor induces photocurrent in the sensor channel which can be used to significantly improve the sensitivity and detection limit of NO_2 sensing.

The observed improvement of MoS_2 sensor performance is associated with enhancement of the current in MoS_2 channel induced by photoexcitation of electron-hole pairs across the direct band gap of single-layer MoS_2. Here, we utilized Au as a metal to provide the electrical contacts to the MoS_2 channel, but recent theoretical study and related experiments suggested that this most common metal may be inefficient for electron injection into single-layer MoS_2.[39] Other metals, such as Ti, were suggested as alternatives, but also graphene was proposed and experimentally tested as an atomically thin contacting layer ideally matching 2D structure of MoS_2.[40−42] Thus, two additional variations of MoS_2-based optoelectronic NO_2 sensors were fabricated and tested. In the first variation, gold electrodes were substituted by graphene, resulting in a Gr−MoS_2−Gr sensor (Figure 4a, inset; Figure S6); in the second variation, graphene electrodes were protected from the exposure to NO_2 gas by applying a top Cr/Au (5 nm/50 nm) coating, resulting in a Au/Gr−MoS_2−Gr/Au type sensor (Figure 4b, inset).

As shown in Figure 4, both device configurations involving graphene electrodes show more than 3 orders of magnitude higher current under the incident red LED illumination power of 60.9 nW (per 10 μm by 10 μm sensor area) when compared to absence of light. The highest dark- and photocurrents are observed for the device with bare graphene electrodes. Among the devices with three types of electrodes, the device with Au electrodes (Au−MoS_2−Au) shows the lowest current (Figure 2 and Figure S1). We ascribe this to a higher work function of Au (5.1 eV) compared to the work function of pristine graphene (4.5−4.6 eV);[17] however, the latter can increase to 5.0 eV and higher[43] as graphene is commonly p-doped due to nanofabrication processes, such as copper etching, lithography, and O_2 plasma etching. Assuming that the currents are limited by the height of the Schottky barrier Φ_{SB} at the electrode−MoS_2 interfaces, the ratio of the currents in the case of Au (I_{Au}) and graphene (I_{GR}) can be used for rough estimation of the Schottky barrier height differences in the approximation of thermionic emission model:[17,44] $\Delta\Phi_{SB} = \Phi_{SB}(Au) - \Phi_{SB}(Gr) = (k_BT/e) \times \ln(I_{Au}/I_{GR}) \approx 0.12$ eV, where k_B and e are Boltzmann constant and elementary charge of electron, respectively. For the case of Au-coated graphene, a smaller Schottky barrier difference $\Delta\Phi_{SB} = \Phi_{SB}(Au) - \Phi_{SB}(Gr/Au)$ of 0.07−0.08 eV was obtained, which can be explained by the influence of bulk layer of Au on the work function of graphene shifting the work function of the Au-coated graphene closer to the Au work function. The results of photoconductivity and NO_2 gas sensing were obtained from 4 to 5 devices with each type of electrode. MoS_2 devices with graphene electrodes show the highest photoresponsivity in the range of 30−150 A/W, which is on the high end of the photoresponsivities reported in literature for MoS_2-based devices.[45,46] With increasing Schottky barrier height, the photoresponsivity decreases to values of 3−12 A/W for the case of Gr/Au electrodes and to 0.2−0.34 A/W for the case of Au electrodes as measured on several devices of each type.

Figure 5a shows time-dependent photocurrent induced in the MoS_2 channels with graphene electrodes (bare and Au-coated) in a response to the "on" and "off" switching of the LED illumination. In both cases, fast and slow components of the photoresponse can be observed like in the case of the device with Au electrodes (Figure 2c). In the case of graphene electrodes, the slow component dominates, resulting in large

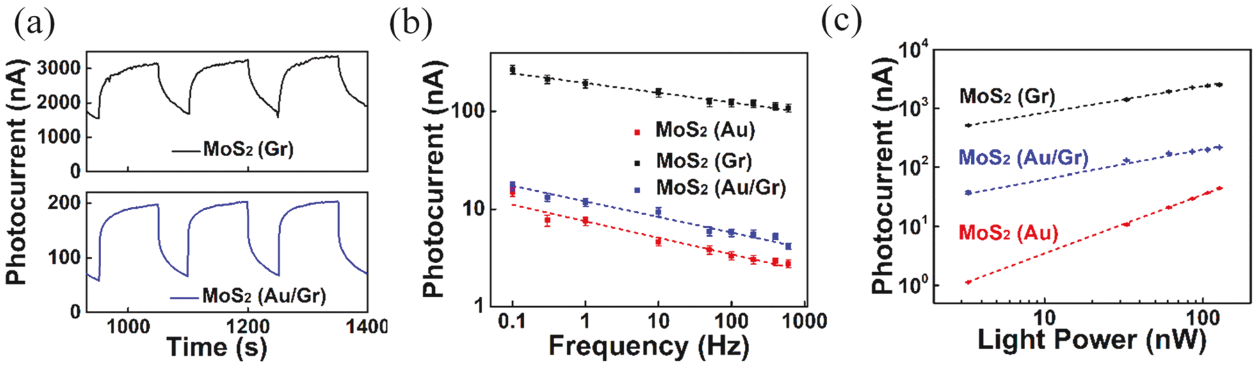

Figure 5. (a) Photocurrent pulses as a response to switching of red LED irradiation "on" and "off" for Gr−MoS_2−Gr (top) and Au/Gr−MoS_2−Gr/Au (bottom) devices. Dependence of photocurrent on (b) frequency of red LED modulation and (c) power of red LED irradiation for MoS_2 devices with three types of electrodes. Dashed lines show power law fits of experimental dependences as described in the text. All data were taken with bias of 5 V.

persistent photocurrent,[47] so the current remains well above its steady-state dark current value during the intervals when the LED irradiation is off.

The dependences of the amplitude of the photocurrent of the MoS_2 devices on the frequency f of square-wave red LED light modulation are presented in Figure 5b and show a decrease of photocurrent with increasing frequency described by power law $I_{ph} \propto f^{-\alpha}$ with best fitting obtained using exponents α of 0.17, 0.1, and 0.16 for the devices with Au, graphene, and graphene/Au electrodes, respectively. Such type of power law dependence of photocurrent with exponent $\alpha < 1$ is well-known in the field of classical photoconductors and is usually associated with wide distribution of photocarrier lifetimes (in our case, from milliseconds to tens of seconds) due to the presence of trap states.[13,46−49] Such traps can be associated with sulfur vacancies responsible for n-type doping, which are typically major defects present in the CVD MoS_2 also.[50,51] Additional trap states may originate from the dangling Si−O bonds at the surface of the SiO_2 substrate, as reported previously.[52,53] Figure 5c shows that the dependence of photocurrent on the incident irradiation power P deviates from direct proportionality and is best described by the power law $I_{ph} \propto P^{\beta}$, similar to the recent reports,[19] with the exponents β values less than unity of 0.63, 0.45, and 0.50 for the devices with Au, graphene, and graphene/Au electrodes, respectively. Such $\beta < 1$ values are also typically associated with the presence of trap states distributed in energy within the band gap of the conventional photoconductors.[47] In the case of 2D materials with high surface to volume ratio, the effect of trap states on the photoconductivity is often described in terms of photogating when under illumination one type of photocarriers is trapped by lattice defects or impurities.[46,49] Such trapping leads to the spatial charge accumulation and induced electric field, which acts as a gate voltage in conventional FETs shifting the Fermi level of 2D channel to the energy position dependent on the time and intensity of incident radiation.[13,46,47,49] The contribution of photogating can explain the power law dependences of photocurrent on frequency and incident power with exponents α and β less than unity presented in Figure 5. In the case of single-layer MoS_2 channel utilized in this study, the trap states can be formed at the interface of MoS_2 and supporting dielectric (SiO_2) layer or on the top of MoS_2 layer. The fast photoresponse component visible at the moment of LED switching "on" and "off" and at high frequencies of modulation can be attributed to direct photoconductivity while slow component of photoresponse can be associated with photogating; however, the boundary between these two contributions cannot be well-defined.

The devices with graphene and graphene/Au electrodes were evaluated for NO_2 sensing under light. Figure 6a shows the transient normalized resistance change (response) of MoS_2 channel with graphene electrodes (Gr−MoS_2−Gr) to 25 to 200 ppb of NO_2 gas exposure. As illustrated in the figure, the device exhibited a response ($\Delta R/R_{N2}$) of ~16% (from 0.85 to 0.99 MΩ) to as low as 25 ppb NO_2 concentration, the smallest reliably achievable concentration in our setup. Furthermore, the normalized resistance change showed a stronger increase with increasing NO_2 concentration, followed by a full recovery. A similar trend, but of much higher magnitude with faster and fuller recovery to baseline upon exposure to only N_2, was observed in the case of device made of the MoS_2 channel with graphene electrodes protected by a Au layer (Figure 6b).

Figures S4 and S5 (Supporting Information) present the raw resistance data upon exposure to different NO_2 concentrations for the above two types of devices used in Figure 6. Additionally, the baseline photocurrent (in the absence of NO_2 exposure) of Au/Gr−MoS_2−Gr/Au was an order of magnitude lower, 0.8 *vs* 6 μA, when compared to that of the Gr−MoS_2−Gr (bare graphene electrodes) device which is ascribed to higher Schottky barrier caused by the influence of bulk Au layer, as discussed previously.

Figure 6c,d presents the amplitude of the normalized resistance change ($\Delta R/R_{N2}$) as a function of NO_2 concentration (*i.e.*, calibration plot) for Gr−MoS_2−Gr and Au/Gr−MoS_2−Gr/Au devices, respectively. The corresponding analytical characteristics of sensitivity and limit of detection of these devices for NO_2 sensing (calculated the same way as described above) are summarized in Table 1.

The results show that the Au/Gr−MoS_2−Gr/Au device had higher sensitivity (3.3 *vs* 1.3%/ppb) and lower LOD (0.1 *vs* 0.2

Table 1. Analytical Characteristics of Single-Layer MoS_2 Channel Gas Sensors with Different Source−Drain Electrodes for NO_2 Sensing

device/condition	sensitivity, %/ppb	limit of detection, ppb
Au−MoS_2−Au/dark	0.1	18
Au−MoS_2−Au/light	4.9	0.2
Gr−MoS_2−Gr	1.3	0.2
Au/Gr−MoS_2−Gr/Au	3.3	0.1

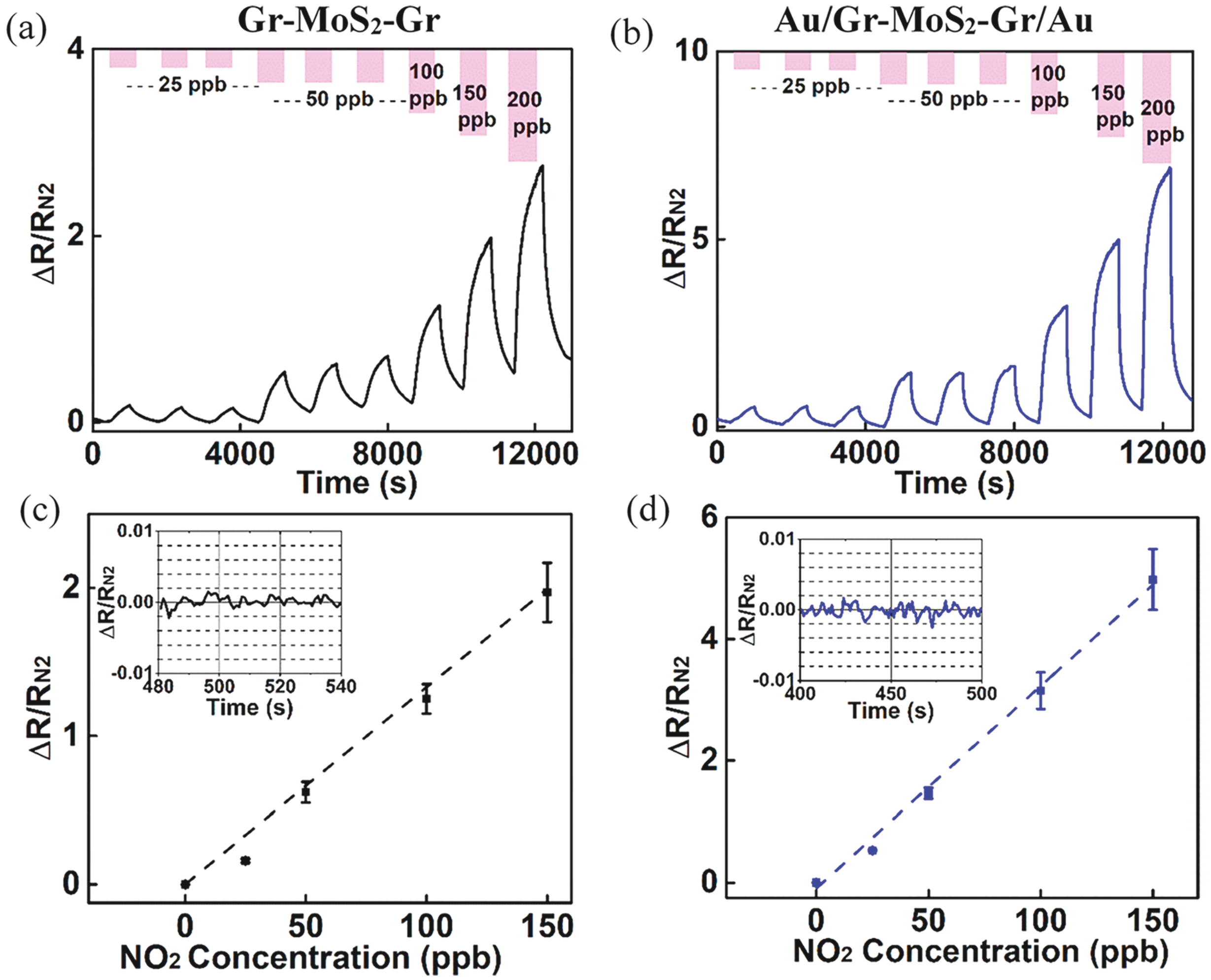

Figure 6. Effect of NO_2 gas exposure at concentrations from 25 to 200 ppb under red light on normalized resistance of (a) Gr−MoS_2−Gr and (b) Au/Gr−MoS_2−Gr/Au devices. Dependence of the normalized amplitude of resistance change of Gr−MoS_2−Gr (c) and Au/Gr−MoS_2−Gr/Au (d) devices on the concentration of NO_2 gas. Inset shows a temporal trace of experimentally recorded noise of $\Delta R/R_{N2}$. All data were collected under dc bias of 5 V.

ppb) compared to Gr−MoS_2−Gr device. We should note that MoS_2-based sensors demonstrated long-term stability under many hours of red LED illumination, NO_2 exposure during performance testing, and storage as illustrated in Figure S7.

The band diagram of the MoS_2 channel in the dark is presented in Figure 7a with Fermi level shifted toward conduction band for typically n-type doped MoS_2. Because of the relatively large band gap of MoS_2 and high Schottky barriers at the metal electrode/MoS_2 interfaces the concentration of free carriers is very low with thermally excited electrons and holes acting as majority and minority carriers, respectively. The relatively low sensitivity of the sensor in the dark can be explained by the presence of oxygen which traps the thermally excited electrons in MoS_2 channel leading to further reduction of the device current. Thus, most of electrons are blocked by oxygen from interacting with NO_2 molecules resulting in suppressed response to the analyte. As schematically illustrated in Figure 7b, under red light illumination the population of free electrons increases by several order of magnitude.

Part of this increase can be due to photogating[46,49] when photoexcited holes are trapped at the MoS_2/SiO_2 interface, generating a spatial positive charge which shifts the Fermi level closer to the edge of conduction band, resulting in increasing population of the thermally excited electrons. These extra electrons are not blocked by oxygen and available for interaction with NO_2 molecules because of the single-layer structure of MoS_2 when any charge carrier is at the surface. As discussed in the literature, NO_2 gas molecules absorbed on MoS_2 channel surface act as electron acceptors and capture the photoexcited electrons, thus leading to a decrease of current (photocurrent) in the channel.[17,29]

Substitution of Au with graphene results in decreasing Schottky barrier height and improving current injection which leads to higher photocurrent. However, due to its high surface area to volume ratio, graphene provides a high density of binding sites for NO_2 gas molecules. It has been reported that the work function of single-layer graphene and the height of the Schottky barrier at MoS_2/graphene interface can be affected by NO_2 exposure,[54,55] which may lead to observed decreasing sensitivity of MoS_2(Gr) as compared to the other types of electrodes. In addition, trapping of NO_2 molecules on the high surface area graphene electrodes can be a cause of more slow recovery after the exposure than in the case of Au/Gr−MoS_2−Gr/Au device as observed in Figure 6. The exposure of the contact layer to the analyte can also serve as an additional source of noise which can be eliminated in a case

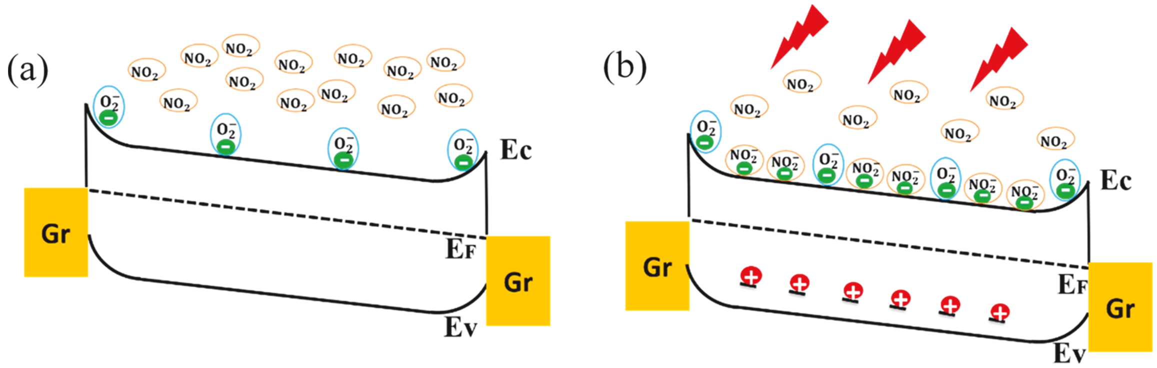

Figure 7. Band diagram of the device showing interaction of conduction band electrons in MoS_2 with NO_2 gas molecules (a) in the dark and (b) under red light illumination.

Table 2. Comparison between Reports on MoS_2-Based NO_2 Gas Sensors and Present Work

material	temperature	minimum concentration tested	detection limit (calculation)	sensitivity, %/ppm	ref
MoS_2	RT	100 ppm	20 ppm	1.37/ppm	16
MoS_2	RT	20 ppb	10 ppb	194/ppm	17
MoS_2	RT	120 ppb	25 ppb	90/ppm	19
Gr/MoS_2	150 °C	1.2 ppm	1.2 ppm	3/ppm	20
MoS_2	RT (UV)	5 ppm	1−5 ppm	0.12/ppm	29
MoS_2	100 °C	5 ppm	1−5 ppm	0.06/ppm	29
MoS_2/Gr	200 °C	50 ppb	14 ppb	18/ppm	30
3D MoS_2	200 °C	50 ppb	28 ppb	20/ppm	31
MoS_2 nanowire	60 °C	1 ppm	4.6 ppb	2.65/ppm	34
PtNPs/MoS_2	RT	0.5 ppm	2 ppb	11/ppm	56
MoS_2	100 °C	25 ppb	2 ppb	0.18/ppm	57
MoS_2	RT (red light)	25 ppb	0.1 ppb	3.3/ppb (3300/ppm)	this work

of graphene electrode protected from NO_2 exposure by Au layer.

As discussed above, the encapsulation of graphene electrodes with Au layer affects the work function of graphene resulting in increasing Schottky barrier height and decreasing photocurrent. On the other hand, it protects the device from the negative effects originated from interaction of graphene electrodes with NO_2 molecules such as decreasing sensitivity due to modulation of work function and a slow sensor recovery. The encapsulation of graphene may also improve the long-term stability of the optoelectronic gas sensor which will be evaluated in our future studies.

Table 2 summarizes state of the art parameters reported in literature for MoS_2-based NO_2 gas sensors.[16,17,19,20,29−31,34,56,57] The optoelectronic MoS_2 sensor operating under red LED light illumination presented in this work shows the highest reported sensitivity to low dosage of NO_2 gas because the photocurrent is used to enhance the sensor response. The calculations following IUPAC defined procedure gave extremely low detection limit in sub-ppb range (0.1 ppb) well suited to U.S. EPA needs for NO_2 sensing at ppb level.

CONCLUSION

Red LED illumination with photon energy matching the direct band gap of the single-layer MoS_2 allowed to use induced photocurrent instead of dark current as a tool for NO_2 gas sensing. The resulted sensor showed extremely high sensitivity to ppb level NO_2 gas exposure up to 3.3%/ppb (3300%/ppm) and sub-ppb limit of NO_2 gas detection at the 0.1 ppb level. The presented concept of enhancing gas sensing performance by inducing a photocurrent can be expanded on different analytes and employ other 2D TMD materials by matching the photon energies to the specific band gaps.

EXPERIMENTAL SECTION

MoS_2 Growth. MoS_2 films were grown by a CVD method using sulfur and molybdenum trioxide (MoO_3) powders as the precursors and sapphire as the substrate. The growth was carried out in a two-zone tube furnace in 50 sccm of argon under ambient pressure. Temperature at the center of the furnace, where the substrate was positioned above MoO_3 powder, was increased to 650 °C at a ramp rate of 25 °C min^{-1}. Sulfur was introduced to the system by evaporation using a heating jacket at 170 °C as soon as the furnace was turned on. The temperature remained constant at 650 °C for 10 min to complete the growth after the furnace and the heating jacket were turned off, and the system was naturally cooled to room temperature.

Graphene Growth. We employ the method reported in our recent publication to produce continuous graphene film.[58] In brief, a 2 × 5 cm^2 piece of polycrystalline copper foil was used as the growth substrate. The copper foil was annealed 1030 °C in the presence of H_2 (10 sccm) and argon (300 sccm) for 2 h in 1 in. quartz tube furnace. Diluted CH_4 in argon (90 ppm) was introduced for 1 h at a flow rate of 375 sccm while H_2 flow remained unchanged. The system was then cooled to room temperature under H_2 (10 sccm) and argon (300 sccm).

Device Preparation. *Au–MoS_2–Au Device.* After the growth, MoS_2 on sapphire is spin-coated with polystyrene (PS). (PS/MoS_2) film was delaminated in deionized (DI) water and washed several times with DI water to remove remaining residues. The floating PS/MoS_2 was transferred on a SiO_2(300 nm)/Si, and PS coating was dissolved by immersing the chip in toluene solution at room temperature. Cr/Au electrodes (5 nm/50 nm) were patterned and deposited using standard photolithography procedures and electron-beam metal deposition. The lateral dimensions of MoS_2 channel of 10 μm by 10 μm are defined by the interelectrode spacing and the electrodes width, both of 10 μm. No additional patterning of MoS_2 channel was required due to high MoS_2 layer sheet resistance as the only area between the electrodes is contributing to the device dark- or photocurrents.

Gr–MoS_2–Gr Device. Figures S6a,b presents optical images of the MoS_2 optoelectronic gas sensor with two patterned graphene electrodes of width of 10 μm and separated by 10 μm. Graphene electrodes were fabricated directly on graphene/copper foil using standard photolithography. The unwanted graphene area was removed using reactive ion etching (O_2 plasma). Graphene electrodes were isolated from the copper foil via a common wet transfer technique supported by PMMA film and using 0.2 M APS solution as copper etching solution. The floating PMMA/graphene electrodes film was washed multiple times with DI water to remove any residue. This PMMA/graphene electrode film was transferred onto a MoS_2 film prepared on Si/SiO_2 substrate. The PMMA layer was then removed in acetone at 60 °C. A small areas of 5 nm/50 nm thick Cr/Au were deposited as electrical contacts using electron-beam metal deposition. Raman spectrum of graphene (Figure S6c) showed strong G peak at 1590 cm^{-1} and 2D peak at 2680 cm^{-1} as compared to very weak D peak at 1350 cm^{-1}, confirming the high quality of graphene and preservation of its properties after the transfer and lithographic electrode patterning.

Au/Gr–MoS_2–Gr/Au Device. For this device structure, another step of photolithography is required to create an overlapping pattern on the existing graphene electrodes. A 5 nm/50 nm thick Cr/Au layer was deposited on top of graphene electrodes using electron-beam metal deposition. For all three structures, a final step of annealing at 200 °C in 15 sccm H_2 and 300 sccm argon was required to remove remaining residues and improve the contact between layers.

Material and Device Characterization. Raman and PL spectra were collected on Horiba LabRam system using a green laser with wavelength of 532 nm and 100× objective (NA = 0.9). The power of the laser beam was fixed at 5 mW to avoid local heating of the materials. Optical image was taken with Hirox KH-7700 digital microscope. SEM imaging was conducted utilizing Zeiss 1540 XB Crossbeam scanning electron microscope.

Electrical and Photoconductivity Measurements and NO_2 Sensing Experiments. The current–voltage (I–V) measurement in the dark and under the light were conducted utilizing a Keithley 236 source-measure unit. The instruments control and data acquisition for all the measurements were conducted utilizing Labview hardware and software. For photoconductivity and gas sensing measurements the red LED (model L10762, Hamamatsu Photonics) with the central wavelength of 660 nm was integrated with the gas sensing mini-chamber. The LED power density was modulated utilizing a function generator DS360 (Stanford Research Systems), and the light intensity on the device was calibrated using silicon photodetector. The frequency dependencies of the photoresponse were studied using a lock-in amplifier (SRS 830, Stanford Research Systems) with the dc bias of 5 V supplied by Keithley 236 source-measure unit, and the circuit including load resistance of 100 kΩ.

For gas sensing experiments, the concentrations of NO_2 gas was regulated by two Alicat Scientific mass flow controllers: one controlling the flow of 99.99% pure N_2 gas and the other controlling the flow of 10 ppm of NO_2 in N_2. The target NO_2 concentration for detection of 25, 50, 100, 150, and 200 ppb were achieved by mixing NO_2 flow with N_2 flow at ratios of 1:399, 2:398, 4:396, 6:394, and 8:392, respectively, while the total flow rate to the sensing chamber remained constant at 400 sccm.

ASSOCIATED CONTENT

Ⓢ Supporting Information

The Supporting Information is available free of charge on the ACS Publications website at DOI: 10.1021/acsnano.8b08778.

Figures S1–S7 show electrical characteristics of the sensors, the dynamics of the sensors' resistance response toward NO_2 gas exposure for the sensors with gold and graphene electrodes in the dark and under red light illumination, the optical imaging of the device and characterization of graphene electrodes, and long-term stability data (PDF)

AUTHOR INFORMATION

Corresponding Authors

*E-mail: misha.itkis@ucr.edu.
*E-mail: adani@engr.ucr.edu.

ORCID

Tung Pham: 0000-0003-0198-0154
Guanghui Li: 0000-0002-0742-9729
Elena Bekyarova: 0000-0001-7565-2773
Mikhail E. Itkis: 0000-0003-2447-2267
Ashok Mulchandani: 0000-0002-2831-4154

Author Contributions

‖T.P. and G.L. contributed equally to this work

Notes

The authors declare no competing financial interest.

ACKNOWLEDGMENTS

This research was funded by grants from the National Science Foundation (1842718 and ECCS-1404671) and UC Riverside and Korea Institute of Materials Science (Research Program (POC2930)) through UC-KIMS Center for Innovation Materials for Energy and Environment. A.M. acknowledges the W. Ruel Johnson Chair in Environmental Engineering.

REFERENCES

(1) Novoselov, K. S.; Geim, A. K.; Morozov, S. V.; Jiang, D.; Zhang, Y.; Dubonos, S. V.; Grigorieva, I. V.; Firsov, A. A. Electric Field Effect in Atomically Thin Carbon Films. *Science* **2004**, *306*, 666–669.

(2) Wang, H.; Yu, L.; Lee, Y. H.; Shi, Y.; Hsu, A.; Chin, M. L.; Li, L. J.; Dubey, M.; Kong, J.; Palacios, T. Integrated Circuits Based on Bilayer MoS_2 Transistors. *Nano Lett.* **2012**, *12*, 4674–4680.

(3) Geim, A. K.; Grigorieva, I. V. Van der Waals Heterostructures. *Nature* **2013**, *499*, 419–425.

(4) Xu, M.; Liang, T.; Shi, M.; Chen, H. Graphene-Like Two-Dimensional Materials. *Chem. Rev.* **2013**, *113*, 3766–3798.

(5) Jariwala, D.; Sangwan, V. K.; Lauhon, L. J.; Marks, T. J.; Hersam, M. C. Emerging Device Applications for Semiconducting Two-Dimensional Transition Metal Dichalcogenides. *ACS Nano* **2014**, *8*, 1102–1120.

(6) Tan, C.; Cao, X.; Wu, X. J.; He, Q.; Yang, J.; Zhang, X.; Chen, J.; Zhao, W.; Han, S.; Nam, G. H.; Sindoro, M.; Zhang, H. Recent Advances in Ultrathin Two-Dimensional Nanomaterials. *Chem. Rev.* **2017**, *117*, 6225–6331.

(7) Sun, Z.; Martinez, A.; Wang, F. Optical Modulators with 2D Layered Materials. *Nat. Photonics* **2016**, *10*, 227–238.

(8) Mak, K. F.; Lee, C.; Hone, J.; Shan, J.; Heinz, T. F. Atomically Thin MoS_2: A New Direct-Gap Semiconductor. *Phys. Rev. Lett.* **2010**, *105*, 136805.

(9) Lee, C.; Yan, H.; Brus, L. E.; Heinz, T. F.; Hone, J.; Ryu, S. Anomalous Lattice Vibrations of Single- and Few-Layer MoS_2. *ACS Nano* **2010**, *4*, 2695–2700.

(10) Radisavljevic, B.; Radenovic, A.; Brivio, J.; Giacometti, V.; Kis, A. Single-Layer MoS_2 Transistors. *Nat. Nanotechnol.* **2011**, *6*, 147–150.

(11) Choi, M. S.; Qu, D.; Lee, D.; Liu, X.; Watanabe, K.; Taniguchi, T.; Yoo, W. J. Lateral MoS_2 p-n Junction Formed by Chemical Doping for Use in High-Performance Optoelectronics. *ACS Nano* **2014**, *8*, 9332–9340.

(12) Wi, S.; Kim, H.; Chen, M.; Nam, H.; Guo, L. J.; Meyhofer, E.; Liang, X. Enhancement of Photovoltaic Response in Multilayer MoS_2 Induced by Plasma Doping. *ACS Nano* **2014**, *8*, 5270−5281.

(13) Lopez-Sanchez, O.; Lembke, D.; Kayci, M.; Radenovic, A.; Kis, A. Ultrasensitive Photodetectors Based on Monolayer MoS_2. *Nat. Nanotechnol.* **2013**, *8*, 497−501.

(14) Zhang, W.; Huang, J. K.; Chen, C. H.; Chang, H. Y.; Cheng, Y. J.; Li, L. J. High-Gain Phototransistors Based on a CVD MoS_2 Monolayer. *Adv. Mater.* **2013**, *25*, 3456−3461.

(15) Yin, Z.; Li, H.; Li, H.; Jiang, L.; Shi, Y.; Sun, Y.; Lu, G.; Zhang, Q.; Chen, X.; Zhang, H. Single-Layer MoS_2 Phototransistors. *ACS Nano* **2012**, *6*, 74−80.

(16) Late, D. J.; Huang, Y. K.; Liu, B.; Acharya, J.; Shirodkar, S. N.; Luo, J.; Yan, A.; Charles, D.; Waghmare, U. V.; Dravid, V.; Rao, C. N. R. Sensing Behavior of Atomically Thin-Layered MoS_2 Transistors. *ACS Nano* **2013**, *7*, 4879−4891.

(17) Liu, B.; Chen, L.; Liu, G.; Abbas, A. N.; Fathi, M.; Zhou, C. High-Performance Chemical Sensing Using Schottky-Contacted Chemical Vapor Deposition Grown Monolayer MoS_2 Transistors. *ACS Nano* **2014**, *8*, 5304−5314.

(18) Li, H.; Yin, Z.; He, Q.; Li, H.; Huang, X.; Lu, G.; Fam, D. W. H.; Tok, A. L. Y.; Zhang, Q.; Zhang, H. Fabrication of Single- and Multilayer MoS_2 Film-Based Field-Effect Transistors for Sensing NO at Room Temperature. *Small* **2012**, *8*, 63−67.

(19) Cho, B.; Kim, A. R.; Yoon, D.; Lee, Y. J.; Lee, S.; Yoo, T. J.; Kang, C. G.; Lee, B. H.; Ko, H. C.; Kim, D. H.; et al. Bifunctional Sensing Characteristics of Chemical Vapor Deposition Synthesized Atomic-Layered MoS_2. *ACS Appl. Mater. Interfaces* **2015**, *7*, 2952−2959.

(20) Cho, B.; Yoon, J.; Lim, S. K.; Kim, D. H.; Park, S. G.; Kwon, J. D.; Lee, Y. J.; Lee, K. H.; Lee, B. H.; Ko, H. C.; et al. Chemical Sensing of 2D Graphene/MoS_2 Heterostructure Device. *ACS Appl. Mater. Interfaces* **2015**, *7*, 16775−16780.

(21) Perkins, F. K.; Friedman, A. L.; Cobas, E.; Campbell, P. M.; Jernigan, G. G.; Jonker, B. T. Chemical Vapor Sensing with Monolayer MoS_2. *Nano Lett.* **2013**, *13*, 668−673.

(22) Kim, J. S.; Yoo, H. W.; Choi, H. O.; Jung, H. T. Tunable Volatile Organic Compounds Sensor by Using Thiolated Ligand Conjugation on MoS_2. *Nano Lett.* **2014**, *14*, 5941−5947.

(23) Wetchakun, K.; Samerjai, T.; Tamaekong, N.; Liewhiran, C.; Siriwong, C.; Kruefu, V.; Wisitsoraat, A.; Tuantranont, A.; Phanichphant, S. Semiconducting Metal Oxides as Sensors for Environmentally Hazardous Gases. *Sens. Actuators, B* **2011**, *160*, 580−591.

(24) Mubeen, S.; Lai, M.; Zhang, T.; Lim, J. H.; Mulchandani, A.; Deshusses, M. A.; Myung, N. V. Hybrid Tin Oxide-SWNT Nanostructures Based Gas Sensor. *Electrochim. Acta* **2013**, *92*, 484−490.

(25) Dey, A. Semiconductor Metal Oxide Gas Sensors: A Review. *Mater. Sci. Eng., B* **2018**, *229*, 206−217.

(26) Fine, G. F.; Cavanagh, L. M.; Afonja, A.; Binions, R. Metal Oxide Semi-Conductor Gas Sensors in Environmental Monitoring. *Sensors* **2010**, *10*, 5469−5502.

(27) Atkinson, R. Atmospheric Chemistry of VOCs and NO_x. *Atmos. Environ.* **2000**, *34*, 2063−2101.

(28) U.S. Environmental Protection Agency. Air Trends Summary Report; https://www3.epa.gov/ttn/naaqs/standards/nox/s_nox_history.html#3 (accessed Feb 5, 2019).

(29) Kumar, P.; Goel, N.; Kumar, M. UV-Activated MoS_2 Based Fast and Reversible NO_2 Sensor at Room Temperature. *ACS Sens* **2017**, *2*, 1744−1752.

(30) Long, H.; Harley-Trochimczyk, A.; Pham, T.; Tang, Z.; Shi, T.; Zettl, A.; Carraro, C.; Worsley, M. A.; Maboudian, R. High Surface Area MoS_2/Graphene Hybrid Aerogel for Ultrasensitive NO_2 Detection. *Adv. Funct. Mater.* **2016**, *26*, 5158−5165.

(31) Long, H.; Chan, L.; Harley-Trochimczyk, A.; Luna, L. E.; Tang, Z.; Shi, T.; Zettl, A.; Carraro, C.; Worsley, M. A.; Maboudian, R. 3D MoS_2 Aerogel for Ultrasensitive NO_2 Detection and Its Tunable Sensing Behavior. *Adv. Mater. Interfaces* **2017**, *4*, 1700217.

(32) Fan, S. W.; Srivastava, A. K.; Dravid, V. P. UV-Activated Room-Temperature Gas Sensing Mechanism of Polycrystalline ZnO. *Appl. Phys. Lett.* **2009**, *95*, 142106.

(33) Park, S.; An, S.; Mun, Y.; Lee, C. UV-Enhanced NO_2 Gas Sensing Properties of SnO_2-Core/ZnO-Shell Nanowires at Room Temperature. *ACS Appl. Mater. Interfaces* **2013**, *5*, 4285−4292.

(34) Kumar, R.; Goel, N.; Kumar, M. High Performance NO_2 Sensor Using MoS_2 Nanowires Network. *Appl. Phys. Lett.* **2018**, *112*, 053502.

(35) Cho, S. Y.; Kim, S. J.; Lee, Y.; Kim, J. S.; Jung, W. B.; Yoo, H. W.; Kim, J.; Jung, H. T. Highly Enhanced Gas Adsorption Properties in Vertically Aligned MoS_2 Layers. *ACS Nano* **2015**, *9*, 9314−9321.

(36) Cho, B.; Hahm, M. G.; Choi, M. S.; Yoon, J.; Kim, A. R.; Lee, Y.; Park, S.; Kwon, J.; Kim, C. S.; Song, M.; Jeong, Y.; Nam, K.; Lee, S.; Yoo, T. J.; Kang, C. G.; Lee, B. H.; Ko, H. C.; Ajayan, P.; Kim, D. H. Charge-Transfer-Based Gas Sensing Using Atomic-Layer MoS_2. *Sci. Rep.* **2015**, *5*, 8052.

(37) Analytical Methods Committee. Recommendations for the Definition, Estimation and Use of the Detection Limit. *Analyst* **1987**, *112*, 199−204.

(38) Lee, K.; Gatensby, K.; McEvoy, N.; Hallam, T.; Duesberg, G. S. High-Performance Sensors Based on Molybdenum Disulfide Thin Films. *Adv. Mater.* **2013**, *25*, 6699−6702.

(39) Popov, I.; Seifert, G.; Tomanek, D. Designing Electrical Contacts to MoS_2 Monolayers: A Computational Study. *Phys. Rev. Lett.* **2012**, *108*, 156802.

(40) Das, S.; Chen, H. Y.; Penumatcha, A. V.; Appenzeller, J. High Performance Multilayer MoS_2 Transistors with Scandium Contacts. *Nano Lett.* **2013**, *13*, 100−105.

(41) Shih, C. J.; Wang, Q. H.; Son, Y.; Jin, Z.; Blankschtein, D.; Strano, M. S. Tuning On-Off Current Ratio and Field-Effect Mobility in a MoS_2-Graphene Heterostructure *via* Schottky Barrier Modulation. *ACS Nano* **2014**, *8*, 5790−5798.

(42) Lee, Y. T.; Choi, K.; Lee, H. S.; Min, S. W.; Jeon, P. J.; Hwang, D. K.; Choi, H.; Im, S. Graphene *Versus* Ohmic Metal as Source-Drain Electrode for MoS_2 Nanosheet Transistor Channel. *Small* **2014**, *10*, 2356−2361.

(43) Yu, Y. J.; Zhao, Y.; Ryu, S.; Brus, L. E.; Kim, K. S.; Kim, P. Tunning the Graphene Work Function by Electric Field Effect. *Nano Lett.* **2009**, *9*, 3430−3434.

(44) Sze, S. M. *Physics of Semiconductor Devices*; Wiley: New York, 1981.

(45) Koppens, F. H. L.; Mueller, T.; Avouris, P.; Ferrari, A. C.; Vitiello, M. S.; Polini, M. Photodetectors Based on Graphene, Other Two-Dimensional Materials and Hybrid System. *Nat. Nanotechnol.* **2014**, *9*, 780−793.

(46) Fang, H.; Hu, W. Photogating in Low Dimensional Photodetectors. *Adv. Sci.* **2017**, *4*, 1700323.

(47) Joshi, N. V. *Photoconductivity: Art, Science, and Technology*; Marcel Dekker, Inc.: NY, 1990; Vol. 25, p 309.

(48) Li, G.; Suja, M.; Chen, M.; Bekyarova, E.; Haddon, R. C.; Liu, J. L.; Itkis, M. E. Visible-Blind UV Photodetector Based on Single-Walled Carbon Nanotube Thin Film/ZnO Vertical Heterostructures. *ACS Appl. Mater. Interfaces* **2017**, *9*, 37094−37104.

(49) Furchi, M. M.; Polyushkin, D. K.; Pospischil, A.; Mueller, T. Mechanisms of Photoconductivity in Atomically Thin MoS_2. *Nano Lett.* **2014**, *14*, 6165−6170.

(50) Cho, K.; Min, M.; Kim, T. Y.; Jeong, H.; Pak, J.; Kim, J. K.; Jang, J.; Yun, S. J.; Lee, Y. H.; Hong, W. K.; Lee, T. Electrical and Optical Characterization of MoS_2 with Sulfur Vacancy Passivation by Treatment with Alkanethiol Molecules. *ACS Nano* **2015**, *9*, 8044−8053.

(51) Qiu, H.; Xu, T.; Wang, Z.; Ren, W.; Nan, H.; Ni, Z.; Chen, Q.; Yuan, S.; Miao, F.; Song, F.; Long, G.; Shi, Y.; Sun, L.; Wang, J.; Wang, X. Hopping Transport Through Defect-Induced Localized States in Molybdenum Disulphide. *Nat. Commun.* **2013**, *4*, 2642.

(52) Guo, Y.; Wei, X.; Shu, J.; Liu, B.; Yin, J.; Guan, C.; Han, Y.; Gao, S.; Chen, Q. Charge Trapping at the MoS_2-SiO_2 Interface and its

Effects on the Characteristics of MoS_2 Metal-Oxide-Semiconductor Field Effect Transistor. *Appl. Phys. Lett.* **2015**, *106*, 103109.

(53) Illarionov, Y. Y.; Rzepa, G.; Waltl, M.; Knobloch, T.; Grill, A.; Furchi, M. M.; Mueller, T.; Grasser, T. The Role of Charge Trapping in MoS_2/SiO_2 and MoS_2/hBN Field-Effect Transistor. *2D Mater.* **2016**, *3*, 035004.

(54) Schedin, F.; Geim, A. K.; Morozov, S. V.; Hill, E. W.; Blake, P.; Katsnelson, M. I.; Novoselov, K. S. Detection of Individual Gas Molecules Adsorbed on Graphene. *Nat. Mater.* **2007**, *6*, 652−655.

(55) Caffrey, N. M.; Armiento, R.; Yakimova, R.; Abrikosov, I. A. Changes in Work Function due to NO_2 Adsorption on Monolayer and Bilayer Epitaxial Graphene on SiC (0001). *Phys. Rev. B: Condens. Matter Mater. Phys.* **2016**, *94*, 205411.

(56) He, Q.; Zeng, Z.; Yin, Z.; Li, H.; Wu, S.; Huang, X.; Zhang, H. Fabrication of Flexible MoS_2 Thin-Film Transistor Arrays for Practical Gas-Sensing Applications. *Small* **2012**, *8*, 2994−2999.

(57) Deokar, G.; Vancsó, P.; Arenal, R.; Ravaux, F.; Casanova-Cháfer; Llobet, E.; Makarova, A.; Vyalikh, D.; Struzzi, C.; Lambin, P.; Jouiad, M.; Colomer, J. F. MoS_2-Carbon Nanotube Hybrid Material Growth and Gas Sensing. *Adv. Mater. Interfaces* **2017**, *4*, 1700801.

(58) Malekpour, H.; Ramnani, P.; Srinivasan, S.; Balasubramanian, G.; Nika, D. L.; Mulchandani, A.; Lake, R. K.; Balandin, A. A. Thermal Conductivity of Graphene with Defects Induced by Electron Beam Irradiation. *Nanoscale* **2016**, *8*, 14608−14616.